

# Critical role of intercalated water for electrocatalytically active nitrogen-doped graphitic systems

Ulises Martinez,<sup>1</sup> Joseph H. Dumont,<sup>1,2</sup> Edward F. Holby,<sup>3</sup> Kateryna Artyushkova,<sup>2</sup> Geraldine M. Purdy,<sup>1</sup> Akhilesh Singh,<sup>1</sup> Nathan H. Mack,<sup>4</sup> Plamen Atanassov,<sup>2</sup> David A. Cullen,<sup>5</sup> Karren L. More,<sup>5</sup> Manish Chhowalla,<sup>6\*</sup> Piotr Zelenay,<sup>1</sup> Andrew M. Dattelbaum,<sup>1</sup> Aditya D. Mohite,<sup>1</sup> Gautam Gupta<sup>1\*</sup>

2016 © The Authors, some rights reserved; exclusive licensee American Association for the Advancement of Science. Distributed under a Creative Commons Attribution NonCommercial License 4.0 (CC BY-NC). 10.1126/sciadv.1501178

Graphitic materials are essential in energy conversion and storage because of their excellent chemical and electrical properties. The strategy for obtaining functional graphitic materials involves graphite oxidation and subsequent dissolution in aqueous media, forming graphene-oxide nanosheets (GNs). Restacked GNs contain substantial intercalated water that can react with heteroatom dopants or the graphene lattice during reduction. We demonstrate that removal of intercalated water using simple solvent treatments causes significant structural reorganization, substantially affecting the oxygen reduction reaction (ORR) activity and stability of nitrogen-doped graphitic systems. Amid contrasting reports describing the ORR activity of GN-based catalysts in alkaline electrolytes, we demonstrate superior activity in an acidic electrolyte with an onset potential of  $\sim 0.9$  V, a half-wave potential ( $E_{1/2}$ ) of 0.71 V, and a selectivity for four-electron reduction of  $>95\%$ . Further, durability testing showed  $E_{1/2}$  retention  $>95\%$  in  $N_2$ - and  $O_2$ -saturated solutions after 2000 cycles, demonstrating the highest ORR activity and stability reported to date for GN-based electrocatalysts in acidic media.

## INTRODUCTION

Graphitic materials (1–6) are widely used for a variety of energy conversion and storage devices such as electrodes in Li-ion batteries, supercapacitors (7, 8), catalyst supports for fuel cells (9, 10), and oxygen reduction reaction (ORR) electrocatalysts (11–13). Nevertheless, further development of carbon materials for energy-related applications suffers from a limited understanding of the design factors that control the formation of high-performing materials. This is mainly due to their complex heterogeneous character. In an effort to address this critical issue, numerous studies have focused on the use of ordered graphitic carbon materials (2–6, 8, 14). Typically, reduced graphene oxide (GO) is used for energy-related applications because it can be produced in sizable quantities and heteroatoms (N, B, and S) and transition metals (Fe, Ni, and Co) can be readily incorporated into the graphene lattice (11, 15, 16). Despite the fact that GO is synthesized and processed in aqueous environments, the role of intercalated water in the resulting structure and chemical composition for energy-related processes is rarely discussed (3, 6, 12, 13, 17, 18). Particularly, the role of water and its impact on structure, morphology, and catalytic activity during reduction of GO are not well understood (19).

Here, we demonstrate, for the first time, the critical role of the removal of intercalated water from within graphene nanosheets in the formation of functional graphitic materials. Removal of intercalated water is achieved using a solvent drying technique based on Hansen's solubility parameters (dispersion,  $\delta_d$ ; hydrogen bonding,  $\delta_H$ ; and po-

larity,  $\delta_p$ ), leading to a significant impact in the GO physical structure, decreasing the interlayer  $d$  spacing, and changing the concentration of functional groups. The decrease in interlayer spacing leads to the emergence of structured water (similar to that observed in ice) at room temperature. Further, as a practical example, we demonstrate the applicability of this phenomenon in the formation of ORR active GO catalysts. In sharp contrast with previous reports demonstrating the ORR performance of GO catalysts only in alkaline media, we report a catalyst that has the highest activity reported to date in acidic media, a technologically relevant pH environment. Our findings suggest that removal of water is the key to the design of next-generation carbon nanomaterials in realizing their full potential for energy applications.

## RESULTS AND DISCUSSION

GO is synthesized in aqueous solutions and even "dry" GO films contain a substantial amount of intercalated water that organizes between the oxygen-functionalized nanosheets (19–22). Here, we use a simple solvent drying technique based on Hansen's solubility parameters to obtain dry GO films with a high degree of ORR catalytic activity. The drying process is shown in Fig. 1A. The GO nanosheets are rinsed with solvents of similar  $\delta_d$  character to but lesser  $\delta_p$  and  $\delta_H$  character than water (for example, ethanol and diethyl ether; see table S1 for  $\delta$  values), and then vacuum-dried to obtain compacted, partially reduced GO. The resulting films are then annealed at 850°C in ammonia to induce nitrogen heteroatoms and simultaneously reduce GO to obtain NrGO (Fig. 1, B and C). STEM images of GO (Fig. 1B and fig. S1) show the presence of intermixed graphitic (dark region) and functionalized (bright region) domains, whereas STEM images of NrGO (Fig. 1C and fig. S1) reveal the presence of largely graphitic domains, suggesting the effective removal of oxygen and the formation of an  $sp^2$  network (23, 24).

<sup>1</sup>Materials Physics and Applications Division, Los Alamos National Laboratory, Los Alamos, NM 87545, USA. <sup>2</sup>Department of Chemical and Biological Engineering, University of New Mexico, Albuquerque, NM 87131, USA. <sup>3</sup>Materials Science and Technology Division, Los Alamos National Laboratory, Los Alamos, NM 87545, USA. <sup>4</sup>Chemistry Division, Los Alamos National Laboratory, Los Alamos, NM 87545, USA. <sup>5</sup>Materials Science and Technology Division, Center for Nanophase Materials Sciences, Oak Ridge National Laboratory, Oak Ridge, TN 37831, USA. <sup>6</sup>Science and Engineering, Rutgers University, 607 Taylor Road, Piscataway, NJ 08854, USA.

\*Corresponding author. E-mail: gautam@lanl.gov (G.G.); manish1@rci.rutgers.edu (M.C.)

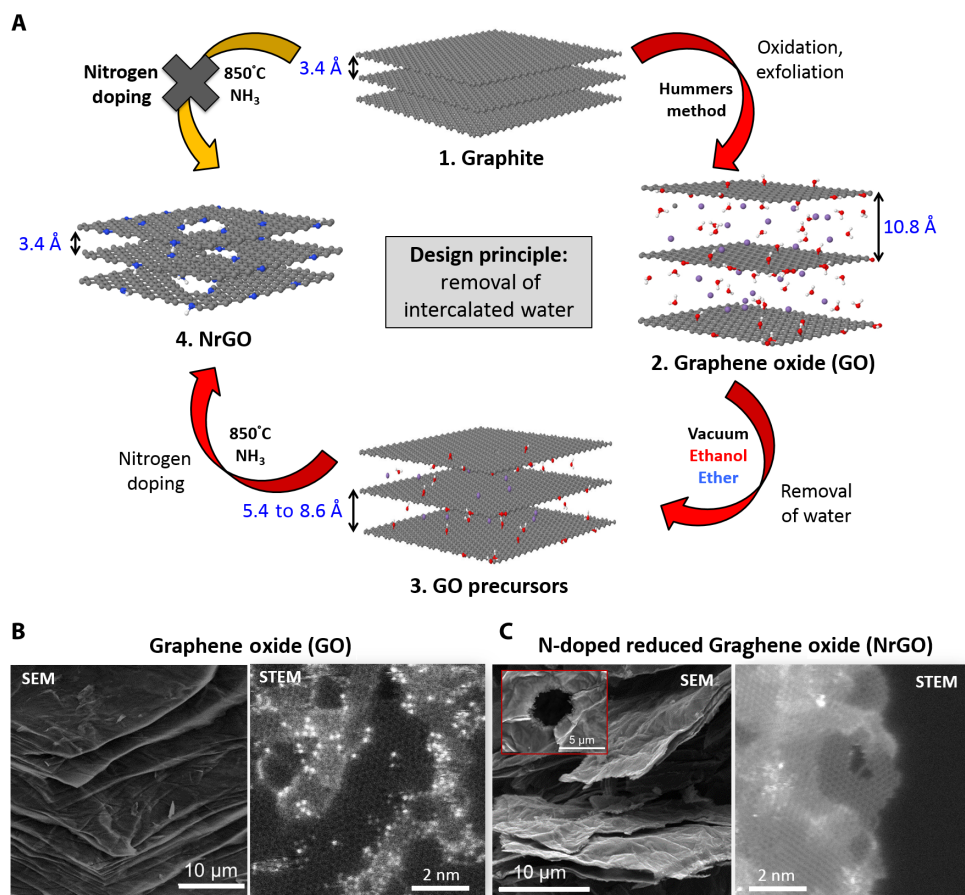


**Fig. 1. Synthesis of nitrogen-doped reduced GO (NrGO) catalysts.** (A) Schematic of the process developed to make NrGO catalysts. Natural graphite (with a  $d$  spacing of 3.4 Å) is chemically functionalized and exfoliated using potassium permanganate and sulfuric acid (modified Hummers method) to produce a GO powder with a  $d$  spacing of  $\sim 1$  nm. GO is then subjected to different solvent-rinsing treatments followed by vacuum drying to effectively remove unbound intercalated water as indicated by the decrease in  $d$  spacing (8.6 to 5.4 Å, depending on solvent used for rinsing). The resulting dried GO is doped with nitrogen ( $\text{NH}_3$  at 850°C), leading to the formation of NrGO catalysts with a final  $d$  spacing of 3.4 Å. Atoms: C (gray), Mn from  $\text{KMnO}_4$  (purple), N (blue), O (red), and H (white). (B and C) Electron micrographs [via scanning electron microscopy (SEM) and scanning transmission electron microscopy (STEM)] of (B) GO and (C) NrGO (ether) showing oxidized and graphitic domains. Brighter atoms correspond to Si atoms, a common graphene impurity (38).

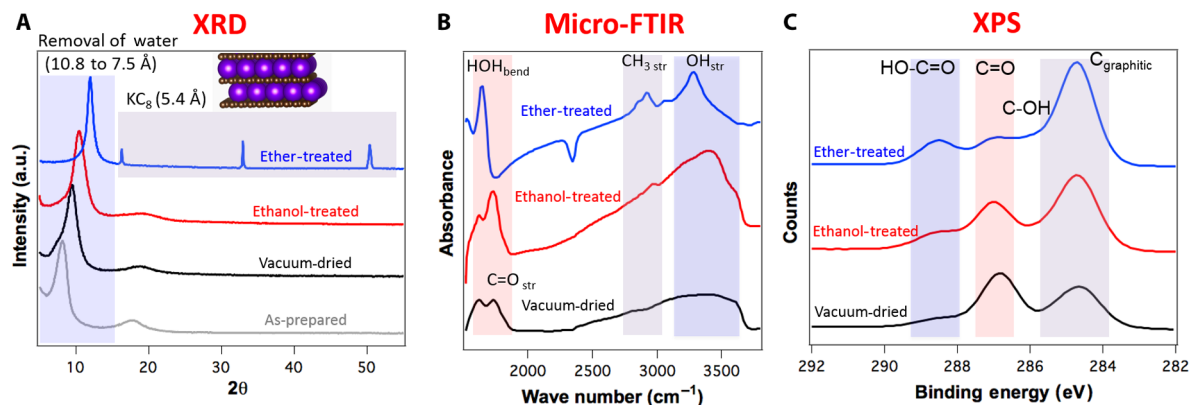


**Fig. 2. Structural and chemical characterization of solvent-treated GO.** (A) XRD patterns show a steady decrease in  $d$  spacing (10.8 to 7.5 Å) and the emergence of a diffraction peak at 5.4 Å ( $\text{KC}_8$ ), as well as its associated higher-order lamellar peaks indicating long-range lamellar order, as a function of the solvent drying technique. The inset shows the  $\text{KC}_8$  structure. K (purple). a.u., arbitrary units. (B) Micro-FTIR (Fourier transform infrared) spectra demonstrating the presence of confined water (sharp  $-\text{OH}$  peak emerging at 3280  $\text{cm}^{-1}$ ). (C) X-ray photoelectron spectroscopy (XPS) data showing an increase in graphitic carbon (284.6 eV) and a decrease in  $\text{C}=\text{O}$  (286.8 eV) content as a function of solvent rinsing.

Intercalated water leads to the expansion of spacing between the GO nanosheets, which can be readily monitored using x-ray diffraction (XRD). Exfoliation and functionalization of graphite to GO increases the interlayer graphene spacing from 3.4 to 10.8 Å (Fig. 2A), due to the formation of oxygen-containing functional groups on the graphene basal plane and simultaneous intercalation of water (fig. S2). Removal of water via vacuum drying results in the decrease of  $d$  spacing to 8.6 Å (Fig. 2A). We observed that immersing the as-prepared GO in ethanol or diethyl ether followed by vacuum drying further decreased the interlayer  $d$  spacing to 7.8 and 7.5 Å, respectively. Thus, solvent drying effectively removes loosely bound intercalated water from GO. In addition to the decreased interlayer distance, well-defined diffraction peaks appeared at  $2\theta$  values of 16.3°, 32.8°, and 50.3° in the ether-treated GO samples corresponding to a  $d$  spacing of 5.4 Å, with second- and third-order reflections at 32° and 51°, respectively. The presence of higher-order peaks suggests that a significant fraction of the dried GO material has substantial long-range order (23). The 5.4 Å spacing in dry GO matches exactly that of aqueous-free  $\text{KC}_8$  (25). Potassium is most likely intercalated during the synthesis of GO using the modified Hummers method that uses potassium permanganate. Further water removal characterization was carried out via thermogravimetric analysis that is included and discussed in the Supplementary Materials (fig. S3).

Micro-FTIR (Fig. 2B) and XPS (Fig. 2C) were used to corroborate the XRD observations and better understand the structural and chemical configuration of solvent-treated GO. A broad infrared (IR) peak extending from  $\sim 2500$  to  $3700\text{ cm}^{-1}$  is assigned to the combination of C–H and O–H stretching modes for as-prepared GO (26). Ethanol-treated and vacuum-dried GO shows a slight sharpening of the vibrational modes in the same region. However, IR spectra of GO treated with ether and subsequent vacuum drying display a well-defined and sharp O–H stretching mode that shifted to  $3280\text{ cm}^{-1}$ . The shift and sharpness of the peak are consistent with those of confined water and are consistent with the structure of ice (fig. S4) (27–29). Furthermore, XPS data (Fig. 2C) reveal a significant increase in  $\text{sp}^2$  C content (284.6 eV), which is correlated to a decrease in C=O fraction (286.8 eV) with decreasing  $d$  spacing in XRD. The  $\text{C}_{\text{gr}}/\text{C}=\text{O}$  ratio increases from 0.8 for vacuum-dried GO to 4 for ether-treated/vacuum-dried GO (Fig. 2C and fig. S5).

Molecular dynamics (MD) models with reactive force field potentials (30, 31) were used to find relaxed GO structures with intercalated water, water with ethanol, and water with ether (Fig. 3; see model details in the Supplementary Materials). Wrinkling of GO, which has previously been observed via atomic force microscopy and scanning tunneling microscopy for GO deposited on highly oriented pyrolytic graphite (32), was found in all three models. The average  $d$  spacing values between GO sheets were calculated to be 10.8, 7.2, and 6.8 Å for the water, water with ethanol, and water with ether models, respectively. These values are in agreement with the decreasing  $d$  spacing trend observed from our experimental XRD data for the respective systems (Fig. 2A), supporting our hypothesis that solvents can substantially alter the structure of water-intercalated GO. Further, the symmetric wrinkling phenomenon and the resulting small  $d$  spacing of the graphene planes were found in only the ether-treated GO, providing a path to form  $\text{KC}_8$  domains in the ether-treated samples.

Nitrogen doping of solvent-rinsed and vacuum-dried GO was achieved by high-temperature ammonia treatment, resulting in the formation of NrGO (table S2). Overall, the two-dimensional (2D) sheet-like structure

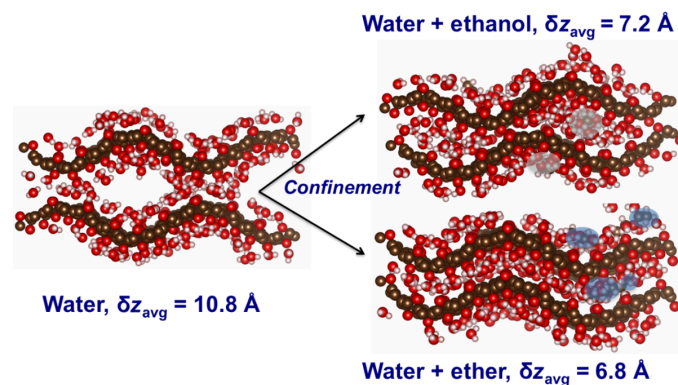


**Fig. 3. Theoretical models of solvent-treated GO structures.** MD relaxed structures for water, water/ethanol, and water/ether. Brown spheres represent carbon atoms, red spheres represent oxygen atoms, and white spheres represent hydrogen atoms. Addition of solvent molecules (highlighted) in between each layer leads to a decrease in  $d$  spacing as observed from XRD data.

of NrGO is preserved after nitrogen incorporation, as seen via SEM (Fig. 4A) and STEM (Fig. 1C and fig. S1). We observed that treatments with ethanol and ether produced NrGO with large (10 to 20  $\mu\text{m}$ ) holes in the graphitic sheets. We hypothesize that the formation of holes might be caused by potassium acting as a pore-forming agent as it sublimes at ca.  $759^\circ\text{C}$  (fig. S6). Another possible hypothesis is related to the confined water molecules. GO structures with decreased  $d$  spacing could prevent water from escaping laterally; thus, upon heating, trapped gases that have evolved (33) could form holes perpendicular to the sheets as they escape. The presence of micrometer-sized holes is beneficial for electrocatalysis because they facilitate transport of reactants and products to and from the active sites throughout the material. Thus, such holey sheets address a significant challenge in using 2D materials for catalysis, that is, inaccessibility of active sites deep within the layered material.

The ORR activity and  $\text{H}_2\text{O}_2$  yield, as determined by RRDE of the NrGO catalysts in an acidic electrolyte (0.5 M  $\text{H}_2\text{SO}_4$ ), are presented in Fig. 4 (B to D). The direct electrochemical reduction of oxygen to water proceeds through a desirable  $4e^-$  transfer ( $\text{O}_2 + 4\text{H}^+ + 4e^- \rightarrow \text{H}_2\text{O}$ ). However, a less efficient  $2e^-$  reaction that generates hydrogen peroxide ( $\text{O}_2 + 2\text{H}^+ + 2e^- \rightarrow \text{H}_2\text{O}_2$ ) can also occur. Therefore, the ORR performance of a catalyst is defined not only by its activity but also by its selectivity for the four-electron reduction of oxygen, and, more importantly, by its half-wave potential ( $E_{1/2}$ ), which is a descriptor of the limiting current density and onset potential of the catalyst. The thermodynamic reversible potential ( $E^\circ$ ) of oxygen reduction at  $25^\circ\text{C}$  is 1.23 V versus the reversible hydrogen electrode (RHE). Any additional potential required to drive the ORR is called the overpotential ( $\eta$ ). Well-performing ORR catalysts are characterized by low  $\eta$ , high  $E_{1/2}$ , and high selectivity values for  $4e^-$  transfer. Here, the as-prepared NrGO catalysts (without solvent or drying pretreatment) showed a high ORR  $\eta$  value of 0.43 V in acidic media. This low activity was accompanied by poor four-electron selectivity, with  $\text{H}_2\text{O}_2$  yield values greater than 50% across the studied range of electrode potentials (Fig. 4C). NrGO catalysts prepared from vacuum-dried and solvent-treated samples showed greatly improved ORR performance, as indicated by a decrease in  $\eta$ , an increase in  $E_{1/2}$ , and a decrease in peroxide yield (Fig. 4, B to D). Ether-treated GO, characterized by a long-range order and decreased  $d$  spacing, was found to be the best oxygen reduction catalyst, with an  $\eta$  of 0.33 V, an estimated  $E_{1/2}$  of 0.71 V,

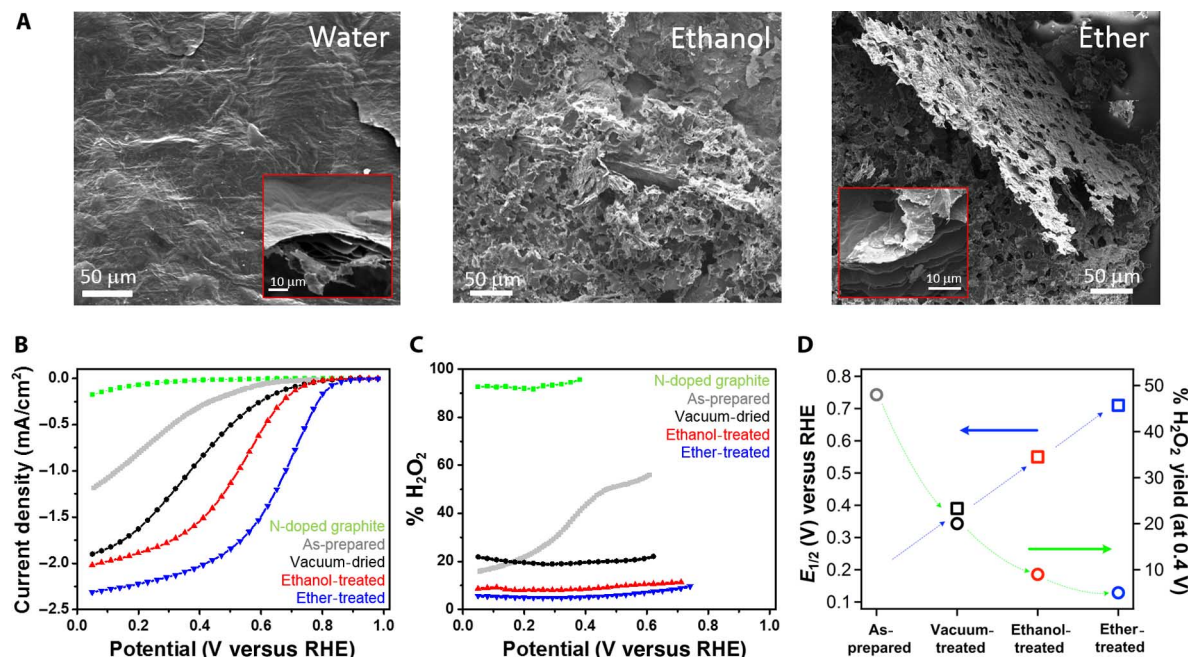


**Fig. 4. Morphological and electrochemical characterization of NrGO catalysts.** (A) SEM images of NrGO catalysts showing sheet-like morphology and micrometer-sized hole formation using solvent-treated GO samples. (B and C) Steady-state step voltammograms of the ORR for all electrocatalysts (B) and corresponding H<sub>2</sub>O<sub>2</sub> yields (C). (D) Summary of  $E_{1/2}$  values and H<sub>2</sub>O<sub>2</sub> yields at 0.4 V. Rotating ring-disc electrode (RRDE) conditions: catalyst loading, 0.6 mg/cm<sup>2</sup>; supporting electrolyte, 0.5 M H<sub>2</sub>SO<sub>4</sub>; rotation rate, 900 rpm; temperature, 25°C; potential steps of 30 mV per step; step duration, 30 s.

and a selectivity for the four-electron reduction of oxygen of ca. 95% (5% H<sub>2</sub>O<sub>2</sub> yield). Figure 4D summarizes our findings highlighting the importance of the solvent treatment process for the development of high-performing ORR GO catalysts: a 300-mV increase in  $E_{1/2}$  from ca. 0.4 V for the vacuum-dried catalyst to ca. 0.7 V for the ether-treated catalyst and a corresponding increase in 4e<sup>-</sup> transfer selectivity from ca. 50% to ca. 95%. These results demonstrate the highest ORR activity reported to date for an NrGO electrocatalysts in acidic media. The vacuum-dried and ethanol-treated NrGO catalysts are discussed in detail in the Supplementary Materials. Further, a reference material, namely, nitrogen-doped graphite, which showed extremely poor ORR activity, demonstrates the advantage of the process developed in this work for the synthesis of active ORR GO catalysts (Fig. 4, B and C).

Additional information on the ORR mechanism on ether-treated NrGO was obtained from the dependence of the oxygen-reduction current on the RRDE rotation rate (Koutecky-Levich relationship) and catalyst loading studies (fig. S7). These studies confirm the predominance of the 4e<sup>-</sup> transfer in the potential range 0 to 0.6 V (versus RHE). Determination of the active site for graphitic ORR electrocatalysts remains a conundrum. Although transition metal impurities inherent from the GO synthesis process (34) were identified from XPS analysis (Supplementary Materials), these impurities were present regardless of the solvent treatment, indicating that the structural and chemical differences arising from solvent treatments are primarily responsible for the improved catalytic activity. Last, accelerated durability testing showed less than 5% loss in the  $E_{1/2}$  value in both N<sub>2</sub>- and O<sub>2</sub>-saturated solutions after 2000 cycles (fig. S8). Elemental analysis using XPS also showed negligible differences among NrGO catalysts after 2000 cycles (fig. S9 and tables S2 and S3).

In summary, we demonstrate active GO catalysts for ORR under acidic conditions through the application of simple solvent drying strategies. These strategies facilitate the efficient removal of the trapped

water within the graphitic sheets, which, in turn, allows for controlling the macroscopic structure and morphology of electrocatalysts upon nitrogen doping. Further advances in catalytic performance from carbon-based catalysts should be obtainable by varying the polarity, miscibility, and wetting properties of solvents, as well as by developing new aqueous-free approaches. The fundamental understanding obtained from our studies should have the potential to establish the design rules for graphene and other related materials such as transition metal dichalcogenides and transition metal oxides.

## MATERIALS AND METHODS

### Synthesis of GO

GO was synthesized via a modified version of the Hummers method (35). In brief, 4 g of graphite powder (Bay Carbon Inc.) was dispersed in 500 ml of 98% H<sub>2</sub>SO<sub>4</sub> using a mechanical stirrer. A total of 16 g of KMnO<sub>4</sub> was added to the mixture over a period of 4 days (4 g/day). The reaction mixture was then quenched with 500 ml of ice-cooled deionized (DI) H<sub>2</sub>O slowly added. About 4 ml of 30% H<sub>2</sub>O<sub>2</sub> was added to the mixture dropwise until the slurry turned yellow. The slurry was then centrifuged until the supernatant became clear. The supernatant was decanted and the precipitated GO was resuspended in H<sub>2</sub>O. The washing process was repeated three times, and the material was then washed in 10% HCl two times, followed by a final wash in DI H<sub>2</sub>O. The final product was resuspended in H<sub>2</sub>O for further use.

### Solvent treatments of GO

Before any solvent treatment, GO-H<sub>2</sub>O suspension was centrifuged to remove excess water. Centrifuged GO was then rinsed with 30-ml aliquots of solvents: water, ethanol, and diethyl ether. The GO-solvent

solution was mixed with a vortex mixer. Solvent-treated GO was then centrifuged at 4000 rpm for 30 min, discarding the supernatant. Solvent-treated GO was then poured onto a vacuum filter funnel (0.2  $\mu\text{m}$  polytetrafluoroethylene filter) and allowed to dry for 5 days. After filtering, the final dried GO film was further dried in a vacuum oven at 40°C for 48 hours.

### Nitrogen doping of GO films

NrGO materials were obtained via simultaneous thermal reduction and nitrogen incorporation using high-temperature ammonia gas treatment. Dried GO films were placed in an alumina crucible inside a quartz furnace tube. The tube was first vented with ultrahigh purity Ar gas [100 standard cubic centimeter per minute (sccm) flow] for 60 min. Ammonia gas was then introduced at 60 sccm, and the temperature was increased to 850°C at a rate of 1°C/min. The furnace temperature was maintained at 850°C for 180 min and then slowly cooled to room temperature.

### Physical and chemical characterization of GO

XRD patterns were measured using a Siemens D5000 diffractometer with Cu K $\alpha$  radiation (1.5418 Å) and a graphite diffracted beam monochromator. The spectra were analyzed using JADE XRD analysis software (Materials Data Inc.). Infrared spectra were obtained using an FTIR spectrometer (Vertex 80, Bruker) combined with an infrared microscope (Hyperion, Bruker), which is equipped with a 15 $\times$  objective and a liquid N $_2$ -cooled MCT (mercury-cadmium-telluride) detector. Four hundred scans with 16 cm $^{-1}$  resolution were averaged for both background and sample spectra. The size of the aperture used in transmission measurements was 100  $\times$  100  $\mu\text{m}$ . All measurements were made at room temperature.

The morphology and structural properties were studied using electron microscopy. SEM images were taken at 5 kV with a FEI Quanta 400 ESEM. High-resolution STEM images were taken using an aberration-corrected Nion STEM (Nion UltraSTEM 200) operated at 60 kV and equipped with Gatan Enfium dual EELS. XPS measurements were performed using a Kratos Axis Ultra DLD x-ray photoelectron spectrometer with a monochromatic Al K $\alpha$  source operating at 150 W with no charge compensation. The survey and high-resolution C 1s and N 1s spectra were acquired at pass energies of 80 and 20 eV, respectively. Three areas per sample were analyzed. Data analysis and quantification were performed using the CasaXPS software. A linear background was used for C 1s, N 1s, and O 1s spectra. Quantification used sensitivity factors that were provided by the manufacturer. A 70% Gaussian/30% Lorentzian line shape was used for the curve fits.

### Electrochemical characterization

Rotating disc electrode measurements of the ORR were performed in a conventional three-electrode cell at a rotating disc speed of 900 rpm and at room temperature using a VMP3 potentiostat (Bio-Logic). Catalyst loading was 0.6 mg cm $^{-2}$ , except for the catalyst loading studies, which ranged from 0.08 to 0.6 mg cm $^{-2}$ . A graphite rod was used as a counter electrode, whereas an Ag/AgCl (3.0 M NaCl, 0.230 V versus RHE) was used as a reference electrode. ORR steady-state polarization curves were recorded in an O $_2$ -saturated 0.5 M H $_2$ SO $_4$  electrolyte with a potential step of 30 mV per 30 s.

### Modeling of GO structures

The GO system was modeled as a 24.6 Å  $\times$  42.6 Å graphene sheet composed of 400 C atoms with 100 O atoms distributed randomly with

50 on each side of the sheet, thus generating a structure with 25% O coverage. Two such layers were generated and initially separated by 10.8 Å in a 3D periodic box that is 21.6 Å high, generating two inter-GO gallery spaces with the same initial volume. Packmol (36, 37) was used to randomly initialize 100 water molecules and 2 solvent molecules (in the case of ethanol and ether simulations) in the gallery spaces between GO layers for a total of 200 water molecules and 4 solvent molecules (if included). An equal number of molecules were distributed between layers such that each gallery space had an equal initial solvent density. With an assumed excluded volume due to the GO, the combined density of water and solvent was roughly half that of bulk water, representing the “dried” state of each sample.

Simulations of the relaxed structures were obtained through the use of the dispersion/CHONSSi-Ig reactive force field potential as implemented in ADF. This force field has graphite as a fitting structure and includes dispersion forces, which makes it a good candidate potential set for studying GO/solvent interactions. Each initially generated structure model was relaxed for 40,000 MD time steps of 0.25 fs (total simulated time of 10 ps) using a Velocity Verlet + Berendsen algorithm with a set temperature of 298 K using the ReaxFF module of the ADF molecular modeling suite. Longer time relaxations did not significantly change the relaxed structures. After relaxation, the average spacing as reported in the main text was calculated by finding the average  $z$  component of the C atoms in each layer and taking the difference between the two averages.

### SUPPLEMENTARY MATERIALS

Supplementary material for this article is available at <http://advances.sciencemag.org/cgi/content/full/2/3/e1501178/DC1>

Supplementary Results and Discussion

Table S1. Table of Hansen solubility parameters of selected solvents.

Table S2. Summarized XPS data showing differences in atomic ratio of elements for ether-treated and untreated catalysts.

Table S3. Summarized XPS data showing differences in C and N speciation for ether-treated and untreated catalysts.

Table S4. Summarized calculated BET (Brunauer-Emmett-Teller)-specific surface areas and pore volumes obtained from solvent-treated NrGO catalysts.

Fig. S1. High-resolution STEM images of ether-treated GO and NrGO materials.

Fig. S2. XRD spectra of starting, intermediate, and end products.

Fig. S3. Thermogravimetric analysis of solvent-treated GO samples.

Fig. S4. FTIR attenuated total reflectance spectra of water and ice.

Fig. S5. High-resolution C 1s XPS spectra for treated GO precursors.

Fig. S6. XRD data of ether-treated GO showing the presence of a lamellar KC $_8$  structure at an intermediate temperature (400°C), which disappears at higher temperatures (850°C).

Fig. S7. Koutecky-Levich and electrode loading mechanistic studies for ether-treated NrGO catalysts.

Fig. S8. Tafel and accelerated durability studies for the ORR on NrGO electrocatalysts.

Fig. S9. High-resolution XPS N 1s and Mn 2p spectra for ether-treated and untreated NrGO catalysts.

Fig. S10. N $_2$  adsorption isotherms for solvent-treated NrGO catalysts.

### REFERENCES AND NOTES

- M. Pumera, Graphene-based nanomaterials for energy storage. *Energy Environ. Sci.* **4**, 668–674 (2011).
- F. Bonaccorso, L. Colombo, G. Yu, M. Stoller, V. Tozzini, A. C. Ferrari, R. S. Ruoff, V. Pellegrini, 2D materials. Graphene, related two-dimensional crystals, and hybrid systems for energy conversion and storage. *Science* **347**, 1246501 (2015).
- Y. Li, W. Zhou, H. Wang, L. Xie, Y. Liang, F. Wei, J. C. Idrobo, S. J. Pennycook, H. Dai, An oxygen reduction electrocatalyst based on carbon nanotube-graphene complexes. *Nat. Nanotechnol.* **7**, 394–400 (2012).
- G. Wu, K. L. More, P. Xu, H.-L. Wang, M. Ferrandon, A. J. Kropf, D. J. Myers, S. Ma, C. M. Johnston, P. Zelenay, A carbon-nanotube-supported graphene-rich non-precious

- metal oxygen reduction catalyst with enhanced performance durability. *Chem. Commun.* **49**, 3291–3293 (2013).
5. X. Huang, X. Qi, F. Boey, H. Zhang, Graphene-based composites. *Chem. Soc. Rev.* **41**, 666–686 (2012).
6. B. F. Machado, P. Serp, Graphene-based materials for catalysis. *Catal. Sci. Technol.* **2**, 54–75 (2012).
7. J. Hou, Y. Shao, M. W. Ellis, R. B. Moore, B. Yi, Graphene-based electrochemical energy conversion and storage: Fuel cells, supercapacitors and lithium ion batteries. *Phys. Chem. Chem. Phys.* **13**, 15384–15402 (2011).
8. R. Raccichini, A. Varzi, S. Passerini, B. Scrosati, The role of graphene for electrochemical energy storage. *Nat. Mater.* **14**, 271–279 (2015).
9. H. A. Gasteiger, S. S. Kocha, B. Sompalli, F. T. Wagner, Activity benchmarks and requirements for Pt, Pt-alloy, and non-Pt oxygen reduction catalysts for PEMFCs. *Appl. Catal. B Environ.* **56**, 9–35 (2005).
10. P. Trogadas, T. F. Fuller, P. Strasser, Carbon as catalyst and support for electrochemical energy conversion. *Carbon* **75**, 5–42 (2014).
11. R. Bashyam, P. Zelenay, A class of non-precious metal composite catalysts for fuel cells. *Nature* **443**, 63–66 (2006).
12. G. Wu, K. L. More, C. M. Johnston, P. Zelenay, High-performance electrocatalysts for oxygen reduction derived from polyaniline, iron, and cobalt. *Science* **332**, 443–447 (2011).
13. E. Proietti, F. Jaouen, M. Lefèvre, N. Larouche, J. Tian, J. Herranz, J.-P. Dodelet, Iron-based cathode catalyst with enhanced power density in polymer electrolyte membrane fuel cells. *Nat. Commun.* **2**, 416 (2011).
14. D. Chen, L. Tang, J. Li, Graphene-based materials in electrochemistry. *Chem. Soc. Rev.* **39**, 3157–3180 (2010).
15. F. Jaouen, E. Proietti, M. Lefèvre, R. Chenitz, J.-P. Dodelet, G. Wu, H. Taek Chung, C. Marie Johnston, P. Zelenay, Recent advances in non-precious metal catalysis for oxygen-reduction reaction in polymer electrolyte fuel cells. *Energy Environ. Sci.* **4**, 114–130 (2011).
16. Z. Chen, D. Higgins, A. Yu, L. Zhang, J. Zhang, A review on non-precious metal electrocatalysts for PEM fuel cells. *Energy Environ. Sci.* **4**, 3167 (2011).
17. L. Qu, Y. Liu, J.-B. Baek, L. Dai, Nitrogen-doped graphene as efficient metal-free electrocatalyst for oxygen reduction in fuel cells. *ACS Nano* **4**, 1321–1326 (2010).
18. L. Lai, J. R. Potts, D. Zhan, L. Wang, C. K. Poh, C. Tang, H. Gong, Z. Shen, J. Lin, R. S. Ruoff, Exploration of the active center structure of nitrogen-doped graphene-based catalysts for oxygen reduction reaction. *Energy Environ. Sci.* **5**, 7936–7942 (2012).
19. M. Acik, C. Mattevi, C. Gong, G. Lee, K. Cho, M. Chhowalla, Y. J. Chabal, The role of intercalated water in multilayered graphene oxide. *ACS Nano* **4**, 5861–5868 (2010).
20. H.-P. Cong, J.-F. Chen, S.-H. Yu, Graphene-based macroscopic assemblies and architectures: An emerging material system. *Chem. Soc. Rev.* **43**, 7295–7325 (2014).
21. V. Chabot, D. Higgins, A. Yu, X. Xiao, Z. Chen, J. Zhang, A review of graphene and graphene oxide sponge: Material synthesis and applications to energy and the environment. *Energy Environ. Sci.* **7**, 1564–1596 (2014).
22. S. Cerveny, F. Barroso-Bujans, Á. Alegría, J. Colmenero, Dynamics of water intercalated in graphite oxide. *J. Phys. Chem. C* **114**, 2604–2612 (2010).
23. P. V. Kumar, N. M. Bardhan, S. Tongay, J. Wu, A. M. Belcher, J. C. Grossman, Scalable enhancement of graphene oxide properties by thermally driven phase transformation. *Nat. Chem.* **6**, 151–158 (2014).
24. W. Gao, G. Wu, M. T. Janicke, D. A. Cullen, R. Mukundan, J. K. Baldwin, E. L. Brosha, C. Galande, P. M. Ajayan, K. L. More, A. M. Dattelbaum, P. Zelenay, Ozonated graphene oxide film as a proton-exchange membrane. *Angew. Chem. Int. Ed.* **53**, 3588–3593 (2014).
25. L. M. Viculis, J. J. Mack, O. M. Mayer, H. T. Hahn, R. B. Kaner, Intercalation and exfoliation routes to graphite nanoplatelets. *J. Mater. Chem.* **15**, 974–978 (2005).
26. C. Gong, M. Acik, R. M. Abolfath, Y. Chabal, K. Cho, Graphitization of graphene oxide with ethanol during thermal reduction. *J. Phys. Chem. C* **116**, 9969–9979 (2012).
27. H. Iglev, M. Schmeisser, Ultrafast IR spectroscopy of ice–water phase transition. *J. Mol. Liquids* **154**, 14–17 (2010).
28. M. Schmeisser, H. Iglev, A. Laubereau, Maximum superheating of bulk ice. *Chem. Phys. Lett.* **442**, 171–175 (2007).
29. J. P. Devlin, V. Buch, in *Water in Confining Geometries*, V. Buch, J. P. Devlin, Eds. (Springer-Verlag, Berlin, 2003), pp. 425–462.
30. L. Liu, Y. Liu, S. V. Zybin, H. Sun, W. A. Goddard, ReaxFF-Ig: Correction of the ReaxFF reactive force field for London dispersion, with applications to the equations of state for energetic materials. *J. Phys. Chem. A* **115**, 11016–11022 (2011).
31. N. V. Medhekar, A. Ramasubramaniam, R. S. Ruoff, V. B. Shenoy, Hydrogen bond networks in graphene oxide composite paper: Structure and mechanical properties. *ACS Nano* **4**, 2300–2306 (2010).
32. D. K. Pandey, T. Fung Chung, G. Prakash, R. Piner, Y. P. Chen, R. Reifengerger, Folding and cracking of graphene oxide sheets upon deposition. *Surf. Sci.* **605**, 1669–1675 (2011).
33. S. Eigler, C. Dotzer, A. Hirsch, M. Enzelberger, P. Müller, Formation and decomposition of CO<sub>2</sub> intercalated graphene oxide. *Chem. Mater.* **24**, 1276–1282 (2012).
34. A. Ambrosi, C. Kiang Chua, B. Khezri, Z. Sofer, R. D. Webster, M. Pumera, Chemically reduced graphene contains inherent metallic impurities present in parent natural and synthetic graphite. *Proc. Natl. Acad. Sci. U.S.A.* **109**, 12899–12904 (2012).
35. A. Dimiev, D. V. Kosynkin, L. B. Alemany, P. Chaguine, J. M. Tour, Pristine graphite oxide. *J. Am. Chem. Soc.* **134**, 2815–2822 (2012).
36. L. Martínez, R. Andrade, E. G. Birgin, J. M. Martínez, PACKMOL: A package for building initial configurations for molecular dynamics simulations. *J. Comput. Chem.* **30**, 2157–2164 (2009).
37. J. M. Martínez, L. Martínez, Packing optimization for automated generation of complex system's initial configurations for molecular dynamics and docking. *J. Comput. Chem.* **24**, 819–825 (2003).
38. J. Lee, W. Zhou, S. J. Pennycook, J.-C. Idrobo, S. T. Pantelides, Direct visualization of reversible dynamics in a Si<sub>6</sub> cluster embedded in a graphene pore. *Nat. Commun.* **4**, 1650 (2013).

**Acknowledgments:** We would like to thank the Los Alamos National Laboratory for supporting this work. This work was performed, in part, at the Center for Integrated Nanotechnologies, an Office of Science User Facility operated for the U.S. Department of Energy Office of Science by the Los Alamos National Laboratory (contract DE-AC52-06NA25396) and Sandia National Laboratories (contract DE-AC04-94AL85000). STEM was conducted at Oak Ridge National Laboratory's Center for Nanophase Materials Sciences, a U.S. Department of Energy, Office of Science User Facility. **Funding:** Los Alamos authors acknowledge a Los Alamos Directed Research Grant for funding. **Author contributions:** G.G. and A.D.M. conceived the idea, designed and supervised experiments, analyzed data, and wrote the manuscript. U.M. performed synthesis, characterization, and analysis of data, and co-wrote the manuscript. G.M.P. developed the solvent treatment strategy and along with J.H.D. performed synthesis and characterization of materials. Theoretical contributions were performed by E.F.H. IR data were obtained by A.S. K.A. performed XPS measurements and analysis of data. P.A. conceived loading studies. N.H.M., D.A.C., and K.L.M. contributed to high-resolution STEM imaging. M.C. co-designed the experiments, contributed to data analysis, and co-wrote the manuscript with G.G. and U.M. A.M.D. provided guidance to the project and contributed to the organization of the manuscript. P.Z. provided guidance to the project, analyzed the electrochemical data, and provided insight into the ORR mechanism. **Competing interests:** The authors declare that they have no competing interests. **Data and materials availability:** All data needed to evaluate the conclusions in the paper are present in the paper and/or the Supplementary Materials. Additional data related to this paper may be requested from the authors.

Submitted 27 August 2015

Accepted 14 January 2016

Published 18 March 2016

10.1126/sciadv.1501178

**Citation:** U. Martinez, J. H. Dumont, E. F. Holby, K. Artyushkova, G. M. Purdy, A. Singh, N. H. Mack, P. Atanassov, D. A. Cullen, K. L. More, M. Chhowalla, P. Zelenay, A. M. Dattelbaum, A. D. Mohite, G. Gupta, Critical role of intercalated water for electrocatalytically active nitrogen-doped graphitic systems. *Sci. Adv.* **2**, e1501178 (2016).

This article is published under a Creative Commons license. The specific license under which this article is published is noted on the first page.

For articles published under [CC BY](#) licenses, you may freely distribute, adapt, or reuse the article, including for commercial purposes, provided you give proper attribution.

For articles published under [CC BY-NC](#) licenses, you may distribute, adapt, or reuse the article for non-commercial purposes. Commercial use requires prior permission from the American Association for the Advancement of Science (AAAS). You may request permission by clicking [here](#).

**The following resources related to this article are available online at <http://advances.sciencemag.org>. (This information is current as of March 31, 2016):**

**Updated information and services**, including high-resolution figures, can be found in the online version of this article at:

<http://advances.sciencemag.org/content/2/3/e1501178.full>

**Supporting Online Material** can be found at:

<http://advances.sciencemag.org/content/suppl/2016/03/15/2.3.e1501178.DC1>

This article **cites 37 articles**, 3 of which you can be accessed free:

<http://advances.sciencemag.org/content/2/3/e1501178#BIBL>

*Science Advances* (ISSN 2375-2548) publishes new articles weekly. The journal is published by the American Association for the Advancement of Science (AAAS), 1200 New York Avenue NW, Washington, DC 20005. Copyright is held by the Authors unless stated otherwise. AAAS is the exclusive licensee. The title *Science Advances* is a registered trademark of AAAS